Multi-mode predictive energy management for fuel cell hybrid electric vehicles using Markov driving pattern recognizer

Yang Zhou, Alexandre Ravey, Marie-Cécile Péra

Multi-mode Predictive Energy Management for Fuel Cell Hybrid Electric Vehicles Using Markov Driving Pattern Recognizer

Yang Zhou*, Alexandre Ravey, Marie-Cécile Péra
FEMTO-ST (UMR CNRS 6174), FCLAB (FR CNRS 3539), Univ. Bourgogne Franche-Comté, UTBM
Rue Thierry Mieg, BELFORT, FRANCE.
yang.zhou@utbm.fr; alexandre.ravey@utbm.fr; marie-cecile.pera@univ-fcomte.fr.
* *Corresponding Author.*

Abstract

Considering the changeable driving conditions in reality, energy management strategies for fuel cell hybrid electric vehicles should be able to effectively distribute power demands under multiple driving patterns. In this paper, the development of an adaptive energy management strategy is presented, including a driving pattern recognizer and a multi-mode model predictive controller. In the supervisory level, the Markov pattern recognizer can classify the real-time driving segment into one of three predefined patterns. Based on the periodically updated pattern identification results, one set of pre-optimized control parameters is selected to formulate the multi-objective cost function. Afterwards, the desirable control policies can be obtained by solving a constrained optimization problem within each prediction horizon. Validation results demonstrate the effectiveness of the Markov pattern recognizer, where at least 94.94% identification accuracy can be reached. Additionally, compared to a single-mode benchmark strategy, the proposed multi-mode strategy can reduce the average fuel cell power transients by over 87.00% under multi-pattern test cycles with a decrement of (at least) 2.07% hydrogen consumption, indicating the improved fuel cell system durability and the enhanced fuel economy.

Key words: ***Energy Management Strategy, Driving Pattern Recognition, Model Predictive Control, Fuel Cell Hybrid Electric Vehicle*.**

Nomenclature

ABBRIVATIONS		**SYMBOLS**	
HEV	Hybrid Electric Vehicle	P_d	Power demand on DC bus
ICE	Internal Combustion Engine	P_{fc}	Fuel Cell (net) Power
LVQ-NN	learning vector quantization neural network	P_{bat}	Battery Power
PEMFC	Proton Exchange Membrane Fuel Cell	m_{H_2}	Actual Hydrogen Mass Consumption
FCHEV	Fuel Cell Hybrid Electric Vehicle	m_{equ,H_2}	Equivalent Hydrogen Mass Consumption
FC	Fuel Cell	SoC	Battery State-of-Charge
FCS	Fuel Cell System	V_{DC}	DC Bus Voltage
EMS	Energy Management Strategy	ρ_1, ρ_2, ρ_3	MPC Penalty Factors
DP	Dynamic Programming	$P_{fc_{ref}}$	Fuel Cell Reference Power
GA	Genetic Algorithm	H_P	Prediction Horizon
ECMS	Equivalent Consumption Minimization Strategy	T_l	*l*-step Transition Probability Matrix
MPC	Model Predictive Control	N_T	Total Time Scale of Markov Chain
DPR	Driving Pattern Recognition	s	Total Number of Markov State
MC	Markov Chain	φ	Constant Forgetting Factor
TPM	Transition Probability Matrix	D_φ	Markov Chain Effective Memory Depth
SoC	State-of-charge	L_s/L_u	Sampling/updating window length
NoS	Number of Stop	$r(A,B)$	2-D Correlation Coefficient of $A, B \in R^{m\times n}$
NN	Neural Network	SD	Similarity Vector
QP	Quadratic Programming	ΔSD_{max}	Largest Similarity Discrepancy
MPC-S	Single-mode MPC	I_{max}/I_{max-2}	Index of Largest/Second Largest Element in SD
MPC-M	Multi-mode MPC	SoC_0/SoC_N	Initial/Final Battery SoC
MPC-R	MPC with real driving pattern information	$\overline{\lvert P_{fc} \rvert}$	Absolute Value of Average FC Power Transients

I. Introduction

To cope with environmental issues such as global warming, technique developments on hybrid electric vehicles (HEVs) have gained increasingly growing attentions during last few decades [1], [2]. However, due to the use of internal combustion engines (ICE), the traditional HEVs still lead to the consumption of fossil fuels and the emission of greenhouse gases [3]. Considering the higher system efficiency and zero-emission property of the Proton Exchange Membrane Fuel Cell (PEMFC), fuel cell hybrid electric vehicles (FCHEVs) are becoming the competitive substitution to traditional HEVs in automotive industries [4]. Currently, several technical challenges, such as the hydrogen storage, the durability of the fuel cell system (FCS) and the early stage of the hydrogen refueling infrastructures, still remain the major obstacles in the commercialization process of FCHEVs [5].

1.1. Literature Review

The performance of FCHEVs is highly dependent on its energy management strategies (EMS), which distribute the external power demand towards the FCS and other energy/power sources. To improve the fuel economy and the FCS's durability, the development of the reliable control strategies for FCHEVs has become a hot research topic in the field of transportation electrification in recent years. According to previous researches, existing EMSs can be classified into rule-based strategies and optimization-based strategies. Rule-based strategies refer to a bunch of simple and robust energy distribution algorithms, which are developed based on the operation modes of energy sources [6], [7], fuzzy logic theory [8], [9] and other heuristic rules [10], [11]. However, these predefined rules or the expertise knowledge cannot fully ensure the optimal EMS performance (e.g. fuel economy). In contrast, global optimization based strategies aim at achieving the best performance by minimizing the predefined objective functions, where the dynamic programming (DP) [12], [13] and the genetic algorithm (GA) [14], [15] are two effective approaches in searching for the global optima. However, the required entire trip knowledge and the heavy computational burdens prevent these EMSs being used online. Instead, their results often serve as the offline evaluation benchmarks. Alternatively, many researchers switch their attentions to real-time optimization based EMSs, such as equivalent consumption minimization strategies (ECMS) [16]-[18] and model predictive control (MPC) based strategies [19]-[23]. For example, authors in [16] have proposed a sequential quadratic programming based ECMS (SQP-ECMS) strategy for optimizing the power flow among the fuel cell, the battery and the supercapacitor. By using three dynamic penalty functions, the output behaviors of three power sources can be effectively regulated. The experimental validation results show the proposed strategy can reduce the hydrogen consumption by 2.16% compared to a rule-based strategy. Furthermore, authors in [19] have compared several velocity prediction methods applied to the MPC-based EMS for HEVs, where the radial basis function neural network (RBF-NN) predictor can obtain the highest prediction accuracy among all the predictors. Furthermore, combined with velocity prediction results of the RBF-NN, the MPC-based EMS can achieve 7% of fuel economy improvement compared to the ECMS-based strategy.

Although numerous EMSs have been successfully developed for traditional HEVs, identical strategies cannot be directly applied to FCHEVs due to the huge discrepancies between the ICE and the FCS. Specifically, most control strategies for traditional HEVs only take the fuel economy as the primary optimization objective [11]. However, when devising the EMSs for FC-based HEVs, it is also necessary to pay substantial attentions to enhancing the FCSs' durability. For automotive

applications, the complicated and rapid-changing driving conditions require the onboard PEMFC operating under various conditions, e.g. on-off cycles and frequent load changing conditions [24]. Compared to the stable loading conditions, the FCSs' durability would be greatly threatened when coping with such dynamic loading conditions, eventually leading to the acceleration of the FCS degradation. Additionally, the overlarge FC power transients would lead to other serious problems, including the membrane dehydration, the fuel starvation and the pressure imbalance across the membrane electrolyte, which would dramatically shorten the FCSs' lifetime [11]. Therefore, to slow down the FCS performance degradation caused by the exceeding load changes, the EMSs for FCHEVs should effectively restrict the FC power transients by properly allocating the external power demand among various energy sources. This yields the necessity of developing the multi-objective EMS, which can both reduce the hydrogen consumption and extend the lifetime of FCS.

Furthermore, a common drawback in previous researches is that the EMS parameters are optimized for specific driving cycles (e.g. [8]), which, however, did not fully consider the impacts of various driving patterns. Therefore, to obtain the desirable control performance under variable driving conditions, the adaptive EMSs that can both identify the real-time driving patterns and perform corresponding suitable control policies should be further investigated, which simultaneously brings a challenging task, namely driving pattern recognition (DPR). In fact, numerous efforts have been made for this subject in previous researches. For example, as reported in [25], a support vector machine based driving pattern classifier can effectively categorize the online driving segment into one of four predefined modes with 95.20% accuracy. Besides, a fuzzy logic recognizer established in [26] can classify the real-time drive block into several known patterns. Afterwards, with the pattern identification results, one of DP-optimized rule-based strategies is adopted for online energy allocation of a plug-in HEV. Additionally, to split the power demand between the FCS and the supercapacitor, an adaptive fuzzy EMS combined with a multilayer perceptron neural network pattern recognizer is proposed in [27]. With offline GA-optimized fuzzy membership parameters, the proposed adaptive EMS can achieve reasonable energy distribution under multi-pattern driving cycles. Furthermore, a learning vector quantization neural network (LVQ-NN) based DPR approach is proposed in [28]. To cope with the realistic driving conditions, the online pattern identification results generated by the well-trained LVQ-NN are used to select one of pre-optimized rule-based strategies for splitting the energy flow within the FCHEVs' powertrain.

1.2. Motivation and Contribution

Based on the literature review, following limitations can be found in previous researches.

- DPR accuracy compensating approaches in driving pattern shifting phases need to be further investigated. In most of traditional DPR approaches, the historical driving segment within the specified moving window size (e.g. 150s) is commonly taken as the recognition object [29]. In pattern shifting phases, the measured data within the sampling window may belong to multiple driving patterns. Thus, the driving features (e.g. average speed, maximum acceleration etc.) of the upcoming pattern may be hidden in the evolution of statistics. In this case, the latency before correctly identifying the upcoming driving pattern may decrease the DPR reliability.
- In existing DPR approaches, multiple static driving feature parameters are selected to describe the real-time driving conditions. However, too many feature parameters would increase the computational burden of the online pattern identification process. In contrast, few research focuses on the possibility of identifying driving patterns based on the dynamic velocity-acceleration (v-a) transition behaviors. In fact, each driving pattern has its own (v-a) transition

characteristic. For example, vehicles' speed with smaller magnitude and higher changing rate can be detected in urban regions, while in highway regions, vehicles' speed profiles are associated with larger average and lower changing rate. Therefore, using (v-a) transition characteristics may supply a new solution to DPR problem.

- The adaptive EMSs combining with DPR results and multiple sets of deterministic (or fuzzy) rules are widely adopted in previous researches (e.g. [14], [28] and [30]). To further improve EMS performance, the MPC controller may be an ideal substitution to these pre-optimized rules due to its advanced capacity of handling future system disturbances.

To bridge these research gaps, a MPC-based multi-mode EMS for fuel cell hybrid electric vehicle is proposed in this paper, where the major contributions are listed as follows:

- A novel DPR approach based on Markov Chain (MC) and moving window technique is proposed. Specifically, the MC transition probability matrix (TPM) is used to characterize the (v-a) transition behavior of each driving segment. Afterwards, the pattern identification results can be obtained by quantifying the resemblance between the online estimated TPM and the offline benchmark TPM using 2-D correlation coefficient.
- To compensate for potential DPR accuracy losses during pattern shifting phases, several complementary rules are provided for separating the conflict driving pattern pairs when the quantified TPM similarity discrepancy is not significant enough.
- To realize the multi-mode EMS framework, three sets of MPC control parameters are carefully tuned based on the offline DP-optimized results. Afterwards, with the online DPR results, one set of offline-tuned MPC parameters is selected to handle the power requirement under corresponding driving pattern. According to the forecasted speed profile and the selected control parameters, the multi-objective MPC controller can generate desirable solutions within each optimization horizon by simultaneously taking into account the fuel economy and the FCSs' durability.
- The accuracy and reliability of the MC recognizer are verified under multi-pattern driving cycles. Moreover, the effectiveness of the multi-mode EMS is validated through the performance comparisons with the upper and lower benchmarks in multiple case studies.

1.3. Paper Organization

The rest of this paper is organized as follows: the model of studied FCHEV is introduced in section II. Section III presents the design processes of the Markov driving pattern recognizer, the Elman neural network velocity predictor and the multi-mode model predictive controller. The validation of the proposed multi-mode EMS is conducted in section IV. Finally, the conclusion and the future work directions are illustrated in section V.

II. System Modelling

2.1. Vehicle Powertrain Model

In this study, vehicle structural parameters are extracted from a mid-sized sedan (Toyota Prius, 1998 version) from the open-source software ADVISOR, where the key specifications are listed in table I. Moreover, according to our previous energy-component-sizing methods [31], a FCS with 30kW rated power and an onboard battery pack with 6.4kWh (nominal) energy capacity are selected as the energy sources within the studied powertrain. As shown in Fig. 1(a), the FCS is linked to the DC bus via a unidirectional DC-DC converter, while the battery pack is directly connected to the DC bus. Note both energy sources work together to drive a 150kW three-phase AC induction motor.

When the vehicle is running on a non-horizontal road (Fig. 1(b)), its propulsion power P_{pro} can be

computed by (1) [32]. Meanwhile, the power demand on DC bus P_d should be supplied by the output power of FCS P_{fc} and the battery pack P_{bat}, where such power balance relationships can be expressed by (2) and (3). Note P_{fc} denotes the net power (deliverable part) of the studied FCS [33].

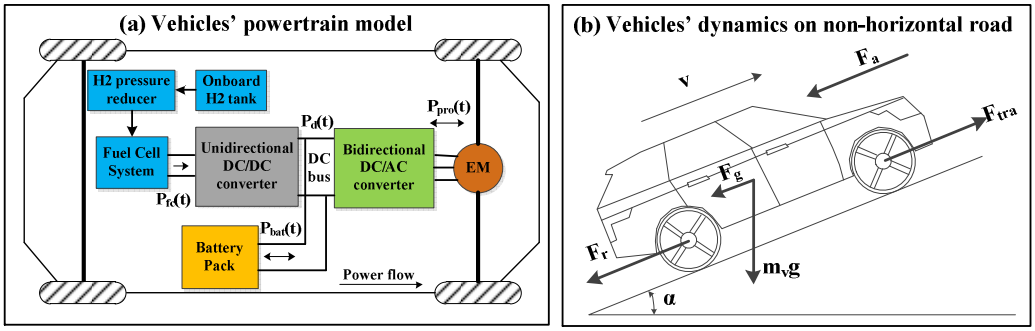

Fig. 1. Vehicle Model: (a) Vehicles' powertrain architectures and (b) vehicles' dynamics on a non-horizontal road.

$$P_{pro}(t) = v(t) \cdot \left(m_v \frac{dv(t)}{dt} + c_r m_v g \cos(\alpha) + m_v g \sin(\alpha) + \frac{1}{2} \rho_a A_f c_d v(t)^2 \right) \quad (1)$$

$$P_d(t) = \frac{P_{pro}(t)}{\eta_{drive}} = P_{fc}(t) \cdot \eta_{DC/DC} + P_{bat}(t) \quad (2)$$

$$\eta_{drive} = \eta_{DC/AC} \cdot \eta_{EM} \quad (3)$$

where m_v and v respectively denote the vehicles' mass and velocity. Moreover, c_r is the rolling friction coefficient, g is the gravitational acceleration, ρ_a is the density of the ambient air, A_f is the area of vehicles' front surface and c_d is the vehicles' aerodynamic coefficient. Besides, the efficiencies of the DC/AC converter and DC/DC converter are assumed as constant, where $\eta_{DC/AC} = 0.95$ and $\eta_{DC/DC} = 0.90$. The road slope α is assumed as zero.

TABLE I. Key specifications of the studied FCHEV powertrain.

Category	Item	Value
Vehicle Parameters	Vehicle Mass	1398 kg
	Vehicle front surface	1.746 m^2
	Air density	1.21 kg/m^3
	Tire radius	0.28 m
	Aerodynamic coefficient	0.3
	Rolling coefficient	0.0135
	Gravitational acceleration	9.81m/s^2
Fuel Cell System	Type	PEMFC
	Rated power	30 kW
	Maximum Efficiency	50.9%
Battery Pack	Type	Lithium-ion
	Energy capacity	6.4kWh
	Nominal DC bus Voltage	320V
Electrical Machine	Maximum Power	150 kW
	Maximum Torque	220 Nm
	Maximum Speed	11000 rpm
DC/DC converter	Efficiency	0.90
DC/AC converter	Efficiency	0.95

2.2. Fuel Cell Model

PEMFC is served as the primary energy source within the hybrid powertrain, where its hydrogen mass consumption $m_{H_2}(t)$ can be calculated by [14]:

$$m_{H_2}(t) = \int_0^t \frac{P_{fc}(t)}{\eta_{fc} \cdot \rho_{H_2}} dt \quad (4)$$

where ρ_{H_2} is the chemical energy density of hydrogen (MJ/kg). Generally, the major losses of a single fuel cell are modeled by the physical and empirical equations (or the polarization curve), which gives the static relationship between the cell voltage and the current density according to the

given operating parameters (e.g. the partial pressure, the humidity and the temperature etc.) [32]. Moreover, the output power of fuel cell stack has to cover the power requirements of all auxiliaries, e.g. the air compressor, the water circulation pump etc. Afterwards, the remaining deliverable part is termed as the net power of the FCS, marked as P_{fc}. In this way, the FCS efficiency η_{fc} is defined by the ratio between the FCS net power and the power generated by the fuel cell stack, where more details regarding the FCS efficiency modeling can be found in previous researches [16],[33]. Specifically, the efficiency curve of the studied FCS is depicted in Fig. 1(c), where the maximum FCS efficiency η_{max} occurs when $P_{fc} = P_{\eta_{max}}$. Besides, the system efficiency will remain above 45% when $P_{fc} \in [P_{\eta_{lower}}, P_{\eta_{upper}}]$, which is defined as the high efficiency region of the studied FCS. To improve the overall system efficiency, FC operating points should be urged towards this region.

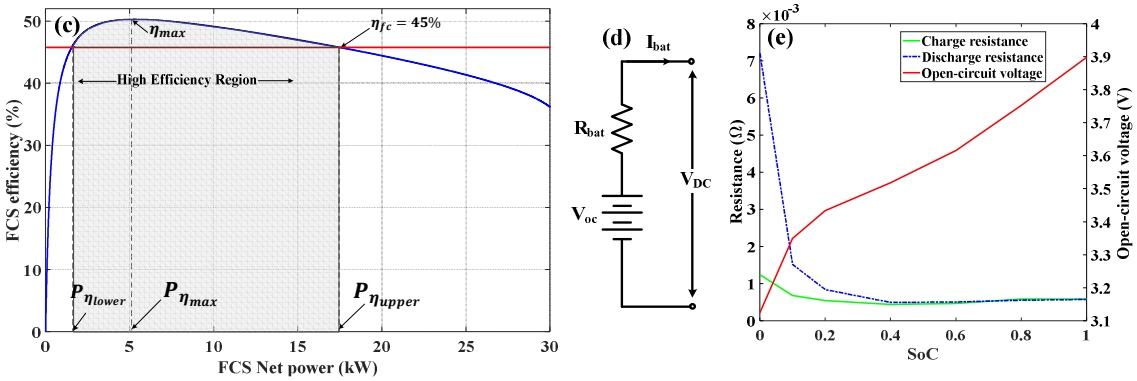

Fig. 1. (c) The efficiency curve of the studied fuel cell system. (d) Equivalent circuit of the internal resistance model (for battery pack). (e) Relationships among open-circuit voltage, internal resistance and battery SoC (for a single cell).

2.3. Battery Model

The battery pack is described by an internal resistance model [34], as shown in Fig. 1(d), where V_{oc}, R_{bat} and V_{DC} respectively denote the open-circuit voltage, internal resistance and DC bus voltage. Besides, the state-of-charge (SoC) denotes the ratio between the remaining battery energy against its fully charged one, where the changing rate of battery SoC, the battery current and the DC bus voltage can be respectively computed by (5a)-(5c).

$$\dot{SoC}(t) = -\frac{\eta_{bat} \cdot I_{bat}(t)}{Q_{bat}} \tag{5a}$$

$$I_{bat}(t) = \frac{V_{oc}(SOC) - \sqrt{V_{oc}(SoC)^2 - 4R_{bat}(SOC)P_{bat}(t)}}{2R_{bat}(SoC)} \tag{5b}$$

$$V_{DC} = V_{oc}(SoC) - I_{bat} \cdot R_{bat}(SoC) \tag{5c}$$

where Q_{bat} denotes the nominal battery capacity, P_{bat} denotes the battery power (negative for charge and positive for discharge) and η_{bat} denotes the battery coulomb efficiency (1 for discharge and 0.98 for charge). In addition, for a single battery cell, its open-circuit voltage and internal resistance change with battery SoC, where such relationships can be found in Fig. 1(e). Note the displayed curves are the characteristic of the 6Ah Li-Ion battery module from Saft Company, which can be found in the database of the ADVISOR software.

2.4. Electrical Machine Model

During vehicles' operations, the electrical machine (EM) supplies the propulsion power required by the driving cycles. In this study, a three-phase induction motor from AC Propulsion Company is used as the calculation model, where its maximum output power is 150 kW and the allowable ranges

of motor rotation speed and torque are respectively from 0 to 11000 rpm and from -220 to 220 N•m. Besides, the working efficiency of the electrical machine can be expressed as a function of motor speed n_{EM} and torque T_{EM}, namely $\eta_{EM} = f_{EM}(n_{EM}, T_{EM})$, where f_{EM} is the mapping function. As shown in Fig. 1(f), the studied motor efficiency map is extracted from the database in ADVISOR. Additionally, given the external power demand, the most efficient EM working point is selected based on its efficiency map.

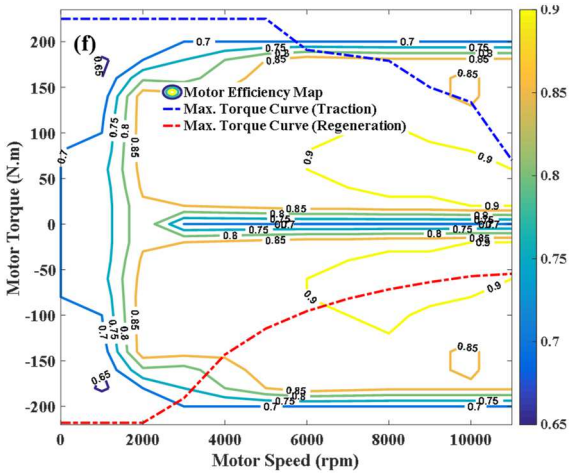

Fig. 1(f). Efficiency Map of the studied electrical machine.

III. Multi-mode Energy Management Strategy

As shown in Fig. 2, the proposed multi-mode EMS consists of a Markov driving pattern recognizer and a multi-mode MPC controller. In the upper level, the MC recognizer can periodically update the pattern identification results, where each driving pattern is related to one set of pre-optimized MPC control parameters. In the lower level, according to the selected control parameters and velocity prediction results, the MPC controller can generate desirable control sequences by solving the constrained optimization problem within each prediction horizon H_p, where the sampling time interval ΔT is specified as one second. Corresponding design process is introduced in the following parts of Section III.

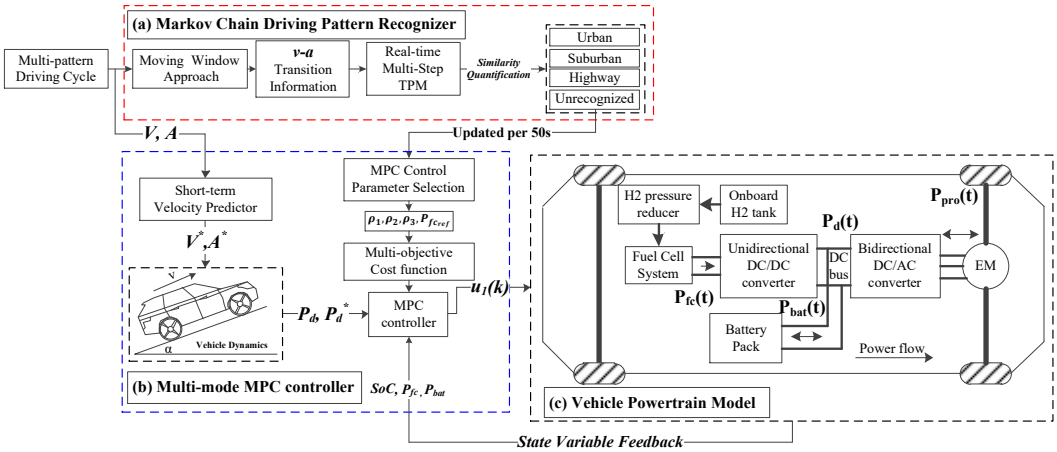

Fig. 2. Schematic Diagram of the multi-mode energy management strategy: (a) Markov Chain based driving pattern recognizer, (b) multi-mode MPC controller and (c) vehicles' hybrid powertrain model.

3.1. Driving Pattern Recognition Approach based on Markov Chain

To discriminate various driving patterns, proper feature parameters that can describe each type of driving condition should be predetermined. In fact, each driving pattern has its own (v-a) transition characteristic. For example, in urban regions, vehicles' average speed is low but the changing rate

is high. In contrast, in highway regions, the average speed is high but the changing rate is low. Therefore, the (v-a) transition behavior is regarded as the feature of each driving pattern, which is quantified by the TPM of Markov Chain in this study. Moreover, the working flow of the proposed DPR approach is given in Fig.3, which includes four working phases: (a) benchmark scenario-based TPMs estimation phase, (b) real-time multi-step TPMs identification phase, (c) similarity degree quantification phase and (d) DPR accuracy compensating phase, where phase (a) is finished offline while others are accomplished online. Detail information about each working phase is introduced in the following parts.

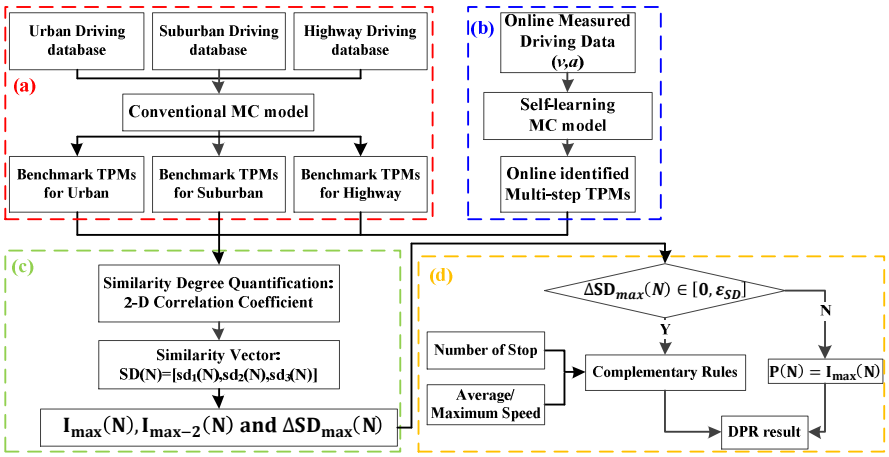

Fig. 3. Working flow of the proposed MC driving pattern recognition approach.

3.1.1. Conventional and Self-learning Markov Model

Two MC models are introduced in this study. Specifically, based on the conventional MC model, numerous standard driving cycles are used to generate the offline benchmark TPMs for three typical driving patterns, namely urban, suburban and highway. Secondly, benefiting from the self-learning MC model, the TPMs reflecting the recent changes of the external driving conditions can be identified using the incrementally measured data. By quantifying the similarity degree between the online estimated TPMs and the offline benchmark TPMs, the real-time driving pattern can be identified.

- Conventional Markov Chain

The MC state is specified as the velocity-acceleration pair in discrete-value domain, marked as $x(k) = \big(v(k), a(k)\big)$, where a countable set $X = \{x_1, x_2, \dots, x_s\}$ is defined as the MC state-space. At $t = k$, given $x(k) \in X$, the probability distribution of MC state at $t = k + l$ is determined by the l-step TPM, namely $T_l \in R^{s\times s}, l = 1,2,\dots,N_T$, where N_T denotes the time scale range of Markov Chain. Its $(i,j)\text{-}th$ element $[T_l]_{ij}$ is a conditional probability reflecting the occurrence of the transition event starting from x_i at time step k and ending at x_j at time step $k + l$, which can be estimated by:

$$[T_l]_{ij} = \Pr\{x(k+l) = x_j | x(k) = x_i\} \approx N_{ij}^l / N_i^l \tag{6}$$

where N_{ij}^l is the number of observed transitions from x_i to x_j after l time steps and N_i^l is the number of transitions starting from x_i, where $N_i^l = \sum_{j=1}^{s} N_{ij}^l, i,j \in \{1,2,\dots,s\}$.

- Self-learning Markov Chain

To identify the real-time TPMs based on incrementally measured data, the conventional TPM model (6) is reformulated into its transition frequency counterpart by [35]:

$$[T_l(k)]_{ij} \approx \frac{N_{ij}^l(k)/k}{N_i^l(k)/k} = \frac{F_{ij}^l(k)}{F_i^l(k)} \tag{7a}$$

$$F_{ij}^{l}(k) = N_{ij}^{l}(k)/k = \frac{1}{k}\sum_{t=1}^{k} f_{ij}^{l}(t) \quad (7b)$$

$$F_{i}^{l}(k) = N_{i}^{l}(k)/k = \frac{1}{k}\sum_{t=1}^{k} f_{i}^{l}(t) \quad (7c)$$

where $F_{ij}^{l}(k)$ is the accumulative frequency $(t = 1\ to\ k)$ of state transition events starting from x_i to x_j after l time steps, while $F_{i}^{l}(k)$ is the frequency of state transition event starting from x_i. Moreover, $f_{ij}^{l}(t)$ is an indicator of state transition events from x_i to x_j and $f_{i}^{l}(t)$ is an indicator of state transition events starting from x_i, where $f_{ij}^{l}(t)$ and $f_{i}^{l}(t)$ equal to 1 only when corresponding transition events occur at time instant t, where $t \in [1, k]$. Otherwise, they both take zero values. According to the definitions of $F_{ij}^{l}(k)$ and $F_{i}^{l}(k)$, they can be further expanded as:

$$\begin{aligned} F_{ij}^{l}(k) &= \frac{1}{k}\sum_{t=1}^{k} f_{ij}^{l}(t) = \frac{1}{k}\left[(k-1)F_{ij}^{l}(k-1) + f_{ij}^{l}(k)\right] \\ &= F_{ij}^{l}(k-1) + \frac{1}{k}\left[f_{ij}^{l}(k) - F_{ij}^{l}(k-1)\right] \\ &\approx F_{ij}^{l}(k-1) + \varphi\left[f_{ij}^{l}(k) - F_{ij}^{l}(k-1)\right] \end{aligned} \quad (8a)$$

$$\begin{aligned} F_{i}^{l}(k) &= \frac{1}{k}\sum_{t=1}^{k} f_{i}^{l}(t) = \frac{1}{k}\left[(k-1)F_{i}^{l}(k-1) + f_{i}^{l}(k)\right] \\ &= F_{i}^{l}(k-1) + \frac{1}{k}\left[f_{i}^{l}(k) - F_{i}^{l}(k-1)\right] \\ &\approx F_{i}^{l}(k-1) + \varphi\left[f_{i}^{l}(k) - F_{i}^{l}(k-1)\right] \end{aligned} \quad (8b)$$

By replacing $1/k$ by the constant forgetting factor $\varphi \in (0,1)$ in (8a) and (8b), all measured transitions $\left[f_{ij}^{l}(1), f_{ij}^{l}(2), \dots, f_{ij}^{l}(k)\right]$ and $\left[f_{i}^{l}(1), f_{i}^{l}(2), \dots, f_{i}^{l}(k)\right]$ can be assigned with a set of exponentially decreasing weights $W = [(1-\varphi)^k, \varphi(1-\varphi)^{k-1}, \dots, \varphi(1-\varphi), \varphi]$, whose all elements add up to 1. In this case, the l-step transition probabilities can be updated by (9).

$$[T_l(k)]_{ij} \approx \frac{F_{ij}^{l}(k-1) + \varphi\left[f_{ij}^{l}(k) - F_{ij}^{l}(k-1)\right]}{F_{i}^{l}(k-1) + \varphi\left[f_{i}^{l}(k) - F_{i}^{l}(k-1)\right]}, i, j = 1,2,\dots,s \quad (9)$$

Note the forgetting factor φ controls the transition probability updating rates, where a larger φ means the higher updating rate. Besides, $D_\varphi = 1/\varphi$ defines the effective memory depth. As reported in [36], the observations within the range $\left[k - D_\varphi + 1, k\right]$ have significant impacts on $[T_l(k)]_{ij}$. In this case, by using a proper forgetting factor φ, corresponding TPMs can be automatically updated online using recently measured data.

3.1.2. Offline Benchmark Transition Probability Matrices Estimation Phase

Overall, the TPM estimation process is illustrated in Fig. 4, where Fig. 4(a) depicts the working flow of offline benchmark TPM estimation phase and Fig. 4(b) presents the working flow of online TPM identification phase. Specifically, three major working steps of the offline TPM estimation phase are given as follows:

Step (1): Numerous standard driving cycles are extracted from the open-source software ADVISOR, namely the HWFET, Cruise3, HHDDT65, ARTEMIS_HW, US06_HW, ARTEMIS_UB, Manhattan, BUSRTE, NurembergR36, AQMDRTC2, WVUINTER, ARTEMIS_SUB, UNIF01, IM240 and WVUSUB. Note the driving cycles with the same pattern are concatenated to form the corresponding sub-database.

Step (2): Combined driving cycle within each sub-database is discretized into numerous (v-a) pairs. These time-labelled driving data are then projected into the V-A plane, where the samples falling into the same rectangle zone are assigned with the identical MC state index.

Step (3): Based on the measurements on the V-A plane, the multi-step TPMs under each driving scenario can be estimated through the conventional MC model (6). These established TPMs are stored as the offline basis for online similarity quantification.

As a result, it can be observed from the 3-D bar diagrams that each driving pattern is associated with

its own (v-a) transition characteristic. In other words, the established multi-timescale TPM groups can be used to characterize corresponding driving patterns.

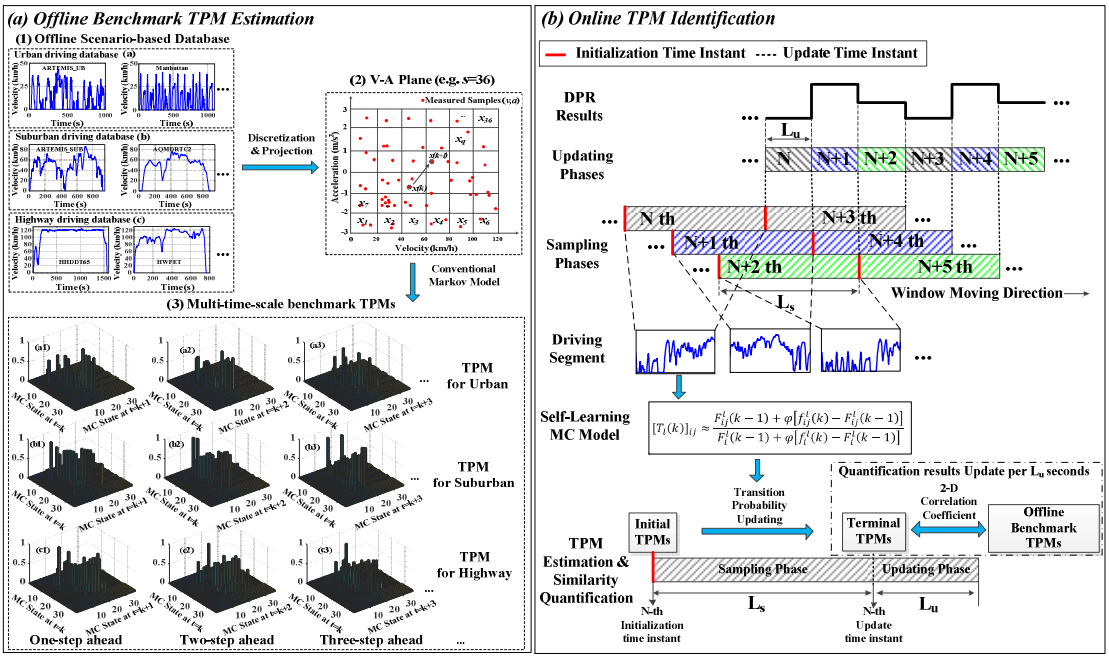

Fig. 4. Working flow of TPM estimation: (a) Offline scenario-based benchmark TPMs estimation phase (e.g. $s = 36$ and $N_T = 3$). (b) Online multi-scale TPM identification phase.

3.1.3. Online Transition Probability Matrices Identification Phase

As can be seen in Fig. 4(b), the self-learning MC model is implemented on each driving segment within the moving window horizon, where L_s and L_u respectively denote the length of sampling and updating window. According to the measured (v-a) data, the transition probabilities can be updated at each sampling time step, thus leading to the evolution of online multi-step TPMs from the initial ones to the terminal ones. Therefore, the resemblance between the real-time identified TPMs and the offline benchmark TPMs is quantified at the end of each sampling phase. Note the similarity quantification results remain unchanged within the entire updating phase (L_u seconds). Afterwards, to quickly eliminate the negative impacts by the old observations, all the elements within the online TPMs are re-initialized to $1/s$ at each initialization time instant (marked as red solid line in Fig. 4(b)). Consequently, the similarity quantification results are updated per L_u seconds, which are then used to finalize the pattern identification results of current driving segment. Note the detail information about the TPM similarity quantification process is given in the subsection 3.1.4.

To ensure the online identified TPMs fully representing the (v-a) transition behaviors within each driving segment, the effective memory depth D_φ of the self-learning MC model is set the same as the sampling window length L_s. Apparently, larger sampling length enables the wider coverage of historical driving conditions. However, the oversized sampling window may contain superfluous information and increase the computational burden as well. As reported in [25], the typical driving period of HEVs is around 3 minutes. In other words, as a reasonable compromise, the sampling window length L_s should be specified as an approximate value to this threshold. Besides, the updating window length L_u should be given a proper value to ensure the updating rate of the real-time DPR results and to avoid the frequent pattern switching. Considering the above-mentioned issues, the sampling window length L_s and the updating window length L_u are respectively set as 150s and 50s. Note these values are obtained through a large amount of cross-validation test.

3.1.4. Similarity Degree Quantification and Complementary Rules

- Similarity Degree Quantification

To quantify the resemblance of the real-time identified TPMs towards the offline benchmark TPMs, the 2-D correlation coefficient $r \in [0,1]$ is introduced. Note $r(A,B)$ is to evaluate the similarity degree between two matrices $A,B \in R^{m\times n}$, which can be computed by

$$r(A,B)=\frac{\sum_{i=1}^{m}\sum_{j=1}^{n}([A]_{i,j}-\bar{A})([B]_{i,j}-\bar{B})}{\sqrt{(\sum_{i=1}^{m}\sum_{j=1}^{n}([A]_{i,j}-\bar{A})^2)(\sum_{i=1}^{m}\sum_{j=1}^{n}([B]_{i,j}-\bar{B})^2)}} \quad (10)$$

where $[A]_{i,j}$ and $[B]_{i,j}$ respectively denote the (i,j)-th element of A and B. $\bar{A}$ and $\bar{B}$ denote the average of the matrix elements. A larger $r(A,B)$ indicates the higher similarity degree between the examined matrix pairs. Besides, let N denotes the index of the updating window. Therefore, at time step $t=k, N=fix(k/L_u)$, where $L_u=50$ and the fix function returns the integer portion of k/L_u.

At $N\text{-}th$ updating time instant, the real-time identified TPMs, marked as $T_l(N)$, are compared with the offline benchmark TPMs, marked as T_l^i, $l=1,2,\dots,N_T$. Note i is the index of the pre-defined driving patterns (1 for urban, 2 for suburban and 3 for highway). Therefore, the quantification results are denoted by a similarity vector $\mathrm{SD(N)}=[\mathrm{sd}_1(\mathrm{N}),\mathrm{sd}_2(\mathrm{N}),\mathrm{sd}_3(\mathrm{N})]$. Note $\mathrm{sd}_i(\mathrm{N})\in[0,1], i=1,2,3$ quantifies the average resemblance of the online estimated TPMs against each type of benchmark TPMs, which can be computed by:

$$sd_i(N)=\frac{1}{N_T}\sum_{l=1}^{N_T} r\left(T_l(N),T_l^i\right), i=1,2,3. \quad (11)$$

Furthermore, let $\Delta\mathrm{SD}_{\max}(\mathrm{N})\in[0,1]$ denotes the difference between the largest and the second largest element in $\mathrm{SD(N)}$, $\varepsilon_{\mathrm{SD}}\in(0,1)$ denotes the preset threshold and $\mathrm{I}_{\max}(\mathrm{N}),\mathrm{I}_{\max-2}(\mathrm{N})\in\{1,2,3\}$ respectively denotes the index of the largest and second largest element in $\mathrm{SD(N)}$. Based on these definitions, there are two possible cases at the end of $N\text{-}th$ sampling horizon:

- **Case I**: If $\Delta\mathrm{SD}_{\max}(\mathrm{N})>\varepsilon_{\mathrm{SD}}$, such similarity discrepancy is considered adequate to separate different driving patterns. Therefore, the real-time driving pattern can be confidently categorized into the one of three modes by $\mathrm{P(N)}=\mathrm{I}_{\max}(\mathrm{N})$. Such quantification result is more likely to happen when the measured (v-a) transitions come from single driving pattern, as shown in the $k\text{-}th$ and $r\text{-}th$ phases in Fig. 5(a).
- **Case II**: If $\Delta\mathrm{SD}_{\max}(\mathrm{N})\le\varepsilon_{\mathrm{SD}}$, it is not convincing to discriminate various driving patterns according to such insignificant similarity discrepancies. This case is more likely to happen during either the driving pattern switching phases (e.g. $q\text{-}th$ phase of Fig. 5(a)) or the confusion phases (e.g. $s\text{-}th$ phase of Fig. 5(a)).

Furthermore, the threshold $\varepsilon_{\mathrm{SD}}$ should be tuned as a tradeoff between the sensitivity to (v-a) transition and the overall DPR accuracy. Specifically, the online DPR results updating rate may be slowed down by a larger $\varepsilon_{\mathrm{SD}}$, leading to the poor real-time practicality towards the changeable driving conditions. On the contrary, if $\varepsilon_{\mathrm{SD}}$ is set too small, frequent pattern switching would reduce the reliability of the proposed DPR approach. After numerous trials and errors, $\varepsilon_{\mathrm{SD}}$ is specified as 0.05 in this study.

In **case II**, TPM similarity quantification results cannot bring a reasonable separation of two conflict patterns (corresponds to the patterns determined by $\mathrm{I}_{\max}$ and $\mathrm{I}_{\max-2}$), which requires additional rules to improve the DPR accuracy. Moreover, different DPR decisions should be made under two possible driving scenarios. Specifically, although $\Delta\mathrm{SD}_{\max}(\mathrm{N})\le\varepsilon_{\mathrm{SD}}$ during pattern switching phases (e.g. Fig. 5(b1), where larger portion of measured data is from "urban" pattern, and Fig. 5 (b2),

where larger portion of measured data is from "suburban" pattern), it is reasonable to set the DPR result as the upcoming "suburban" since the pattern switching moment (marked with the purple dashed curve) exists within the current sampling horizon. As a result, such strategy may improve the pattern identification rate. However, to avoid the mis-recognition in corresponding confusion phases (Fig. 5(c1) and (c2)), it is better to keep the current DPR result as the "urban" since the actual driving pattern does not change.

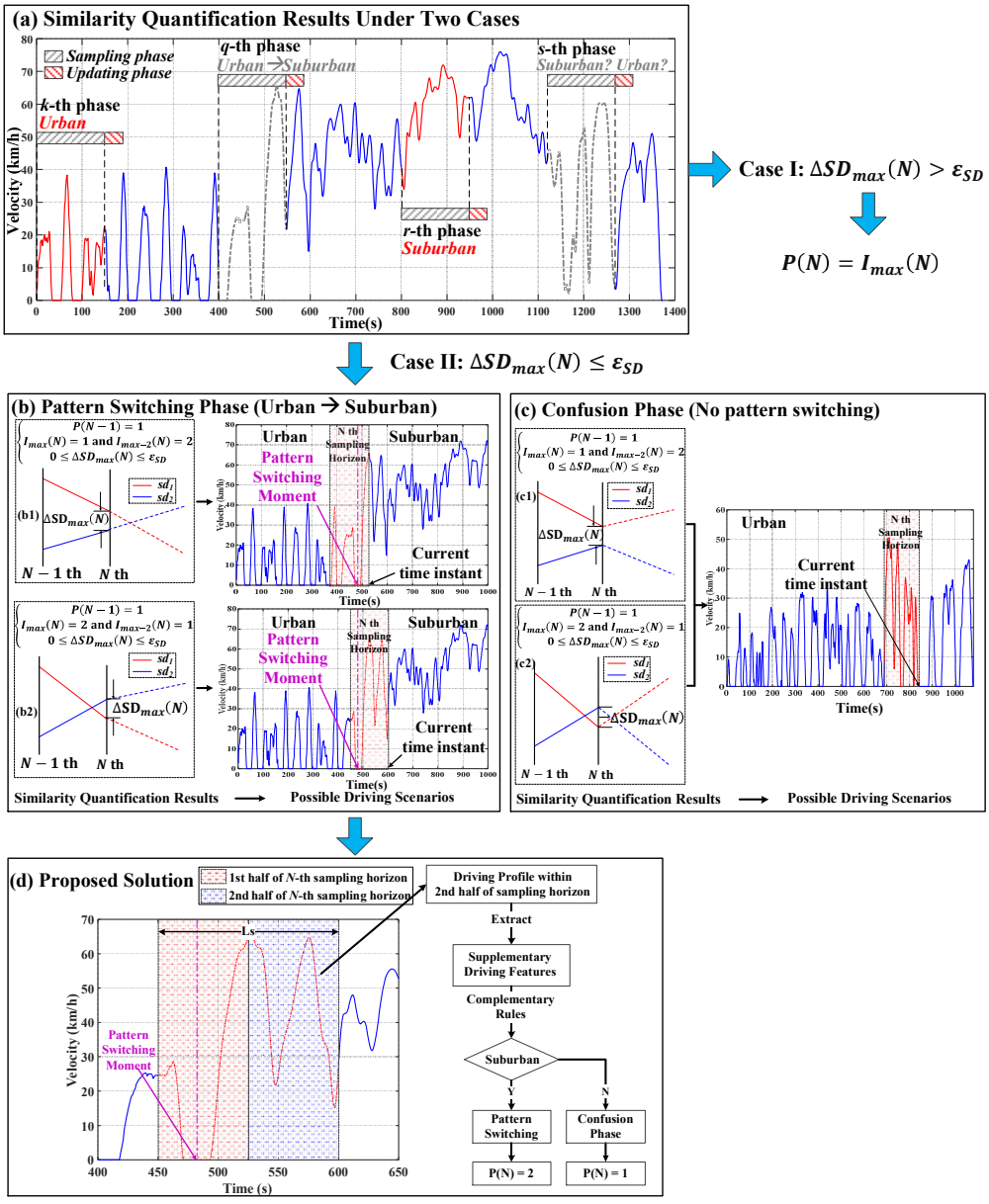

Fig. 5. Working flowing of similarity quantification and DPR accuracy compensate phases: (a) similarity degree quantification results, (b) real driving pattern-switching phases (e.g. urban to suburban), (c) confusion phases and (d) proposed solution to separate pattern switching phases from corresponding confusion phases.

- Complementary Rules

To differentiate the pattern switching phases from corresponding confusion phases, the basic principle of the proposed solution (as shown in Fig. 5(d)) can be stated as follows:

Given (1) $P(N-1) = 1$, (2) $I_{max}(N), I_{max-2}(N) \in \{1,2\}$ and (3) $\Delta SD_{max}(N) \le \varepsilon_{SD}$, the N-th DPR result $P(N)$ should be selected from $I_{max}(N)$ and $I_{max-2}(N)$. Thus, we divide the N-th sampling window into two equal parts. If the driving segment within the second half of sampling horizon has

enough supplementary driving features belonging to "suburban" pattern then $P(N) = 2$. Otherwise, $P(N) = 1$. Similarly, if "urban" and "highway" or "suburban" and "highway" become the conflict pattern pairs, the same strategy can be used to finalize the current DPR results.

To achieve such objective, supplementary driving features should be extracted from the second half of the sampling horizon when $\Delta SD_{max}(N) \leq \varepsilon_{SD}$. Based on the extracted features, the related complementary rules come into effect to judge whether the measured driving fragment can be classified into the upcoming pattern or not.

In the following part, a brief introduction of the supplementary driving feature selection under urban/suburban patterns as well as the establishment of complementary rules is provided to explain the separation criterion of such conflict pattern pairs. The number of stop event (zero-speed) (NoS) and the average speed (v_{mean}) are selected as the supplementary driving features when "urban" and "suburban" become the conflict pattern pairs. To analyze the statistical distributions on the selected features, large amount of driving samples with fixed length are extracted from the offline database, where the length of each sample is the half of entire sampling horizon (75 seconds). Based on these driving samples, the histograms of the statistical distribution on the selected features are given in Fig. 6(a).

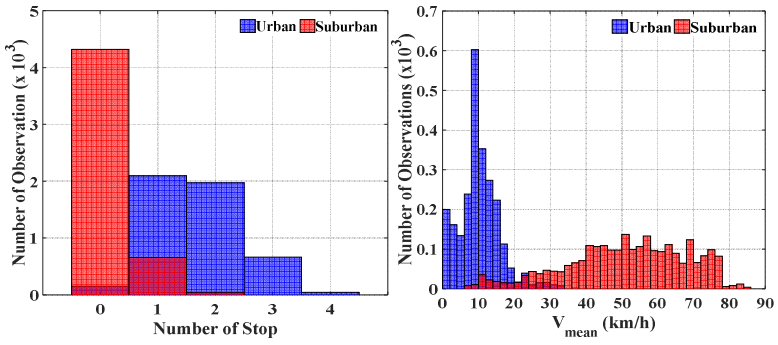

Fig. 6(a). Histogram on NoS and v_{mean} of driving samples (per 75s) under urban and suburban patterns.

TABLE II. Statistical distributions for the supplementary driving features

	$\Pr(NoS = 0)$	$\Pr(NoS = 1)$	$\Pr(NoS > 1)$	$\Pr(v_{mean} > 20km/h)$
UB	3.07%	42.55%	54.38%	4.57%
SUB	86.01%	13.15%	0.84%	95.10%

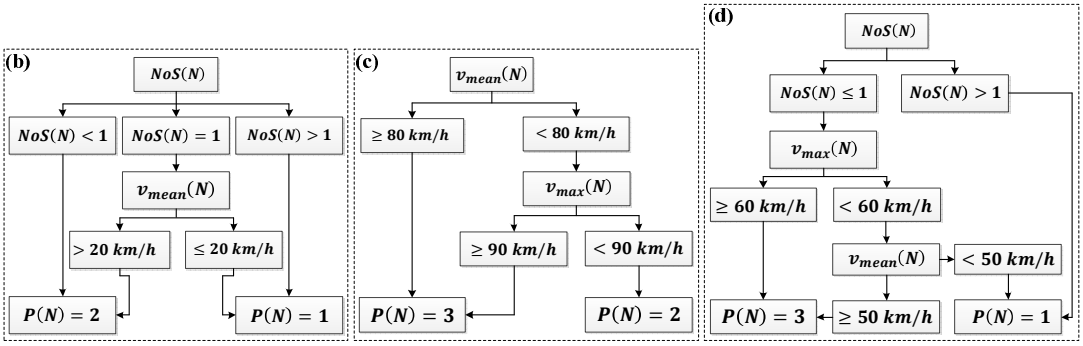

Fig. 6(b)-(d). Complementary rules for (b) urban/suburban, (c) suburban/highway and (d) urban/highway driving conditions.

Moreover, some key figures are listed in table II, where $\Pr(\cdot)$ denotes the probability of the studied event. According to the statistics in table II, the complementary rules to separate urban and suburban patterns are established as shown in Fig. 6(b). Moreover, the complementary rules for urban/highway and suburban/highway can be established in the similar way, where the detail

establishment processes are omitted for simplification purpose. As a result, related complementary rules are given in Fig. 6(c) and (d).

3.2. Elman Neural Network Velocity Predictor

To forecast the speed profile V_k^* required within each MPC rolling optimization horizon, an Elman Neural Network (NN) velocity predictor f_{NN} is adopted, which consists of an input layer, a hidden layer, a content layer and an output layer. Note the content layer can store and feedback the historical information of hidden layer. Based on the historical speed values, future velocity sequence V_k^* can be derived by:

$$V_k^* = \left[v^*(k+1), \dots, v^*\left(k+H_p\right)\right] = f_{NN}\left(v(k-(H_m-1)), \dots, v(k)\right) \quad (12)$$

where H_p is the prediction horizon. Besides, the input size of NN H_m and the number of hidden neuron are respectively set as 10 and 20, as suggested in [19]. After the NN structure is specified, its weights and bias vectors should be tuned to minimize the discrepancies between the actual and expected output in the offline training phase. Note the NN training database is the same database for the benchmark TPMs estimation in section 3.1.2, where 85% and 15% of samples are respectively used for NN training and validating.

3.3. Multi-mode Model Predictive Controller

Model predictive control is a real-time control strategy including three working phases: (1) state trajectory prediction, (2) online cost function minimization, (3) control decision application and state feedback. Such rolling optimization process is repeated at each sampling time instant (1s). The proposed multi-mode MPC is illustrated as follows.

3.3.1. Control Oriented Model

In this study, a linear discrete-time control-oriented model is considered, where its state-space function and the definitions of system variables are given as follows:

$$x(k+1) = A(k)x(k) + B_u(k)u(k) + B_w(k)w(k) \quad (13a)$$

$$y(k) = Cx(k) + D_u u(k) \quad (13b)$$

$$\begin{cases} x(k) &= \left[SoC(k) \;\; P_{fc}(k-1)\right]^T \\ u(k) &= \Delta P_{fc}(k) = \frac{P_{fc}(k) - P_{fc}(k-1)}{\Delta T} \\ y(k) &= \left[SoC(k) \;\; P_{fc}(k)\right]^T \\ w(k) &= P_d(k) \\ r(k) &= \left[SoC_{ref} \;\; P_{fc_{ref}}(k)\right]^T \end{cases} \quad (13c)$$

where $x(k), u(k), y(k), w(k)$ and $r(k)$ respectively denote the state variable, control variable, output variable, measurable disturbance and the reference trajectory. Besides, the discrete form of power balance equation on DC bus can be written as:

$$P_d(k) = P_{fc}(k) \cdot \eta_{DC/DC} + P_{bat}(k) \quad (14)$$

Moreover, a first-order differential equation is used to describe the dynamics of battery SoC:

$$SoC(k+1) = SoC(k) - \frac{\Delta T \cdot \eta_{bat}}{V_{DC}(k) \cdot Q_{bat}} \cdot P_{bat}(k) \quad (15)$$

where $V_{DC}(k)$ is determined by (5c). Based on (13)-(15), the system matrices can be specified as:

$$A(k) = \begin{bmatrix} 1 & \frac{\Delta T \cdot \eta_{DC/DC} \cdot \eta_{bat}}{V_{DC}(k) \cdot Q_{bat}} \\ 0 & 1 \end{bmatrix} \quad B_u(k) = \left[\frac{\Delta T \cdot \eta_{DC/DC} \cdot \eta_{bat}}{V_{DC}(k) \cdot Q_{bat}} \quad 1\right]^T \quad B_w(k) = \left[-\frac{\Delta T \cdot \eta_{DC/DC} \cdot \eta_{bat}}{V_{DC}(k) \cdot Q_{bat}} \quad 0\right]^T$$

$$C = \begin{bmatrix} 1 & 0 \\ 0 & 1 \end{bmatrix} \qquad D_u = [0 \;\; 1]^T \quad (16)$$

3.3.2. Cost function and multi-mode model predictive control

- Cost function and constraints

In this study, three EMS objectives are considered: 1) hydrogen consumption saving, 2) FCS lifetime prolongation and 3) battery SoC regulation. Therefore, at $t = k$, the multi-objective cost function $J(k)$ is formulated as follows:

$$J(k) = \sum_{i=1}^{H_p} [\rho_1(k) \cdot C_1(k+i) + \rho_2(k) \cdot C_2(k+i-1) + \rho_3(k) \cdot C_3(k+i)]$$

$$\begin{cases} C_1(k+i) & = & \left(\frac{P_{fc}(k+i) - P_{fc_{ref}}(k)}{P_{fc_{max}}}\right)^2 \\ C_2(k+i-1) & = & \left(\frac{\Delta P_{fc}(k+i-1)}{\Delta P_{fc_{max}}}\right)^2 \\ C_3(k+i) & = & \left(SoC(k+i) - SoC_{ref}\right)^2 \end{cases} \quad (17)$$

where $P_{fc_{max}} = 30\ kW$ and $\Delta P_{fc_{max}} = 1\ kW/s$. $C_1, C_2, C_3 \in [0,1]$ denote three normalized cost terms and their major functions are given as follows. C_1 is used to urge FC working towards the set points, where the reference value of FC power $P_{fc_{ref}}$ is tuned based on the FCS efficiency curve (see Fig. 1(c)) and different driving patterns. As reported in [24], limiting FC power changing rate ΔP_{fc} is an effective way of enhancing the durability of FCS. Therefore, C_2 is introduced to penalize large FC power transients to slow down its performance degradation caused by exceeding load dynamics. C_3 is introduced to ensure the battery SoC regulation performance. Note the battery pack is not equipped with plug-in technology. Therefore, SoC_{ref} is set the same as the initial SoC value SoC_0 to prevent the battery over-charging or over-discharging, where $SoC_{ref} = SoC_0 = 0.7$. Besides, $\rho_1(k), \rho_2(k), \rho_3(k)$ denote three constant penalty factors, representing the weights on corresponding cost terms. Note the MPC control horizon is set the same length as the prediction horizon, where H_p is set to five. Within each optimization horizon, following constraints have to be satisfied:

$$\begin{cases} 0.55 \le SoC(k+i) \le 0.85 & (18a) \\ 0 \le P_{fc}(k+i) \le 30\ kW & (18b) \\ -1\ kW/s \le \Delta P_{fc}(k+i-1) \le 1\ kW/s & (18c) \\ -50\ kW \le P_{bat}(k+i) \le 100\ kW & (18d) \\ w(k+i) = P_d^*(k+i), i \ge 1 & (18e) \end{cases}$$

The normal operations of FC and battery pack are ensured by constraints (18a)-(18d). Constraint (18e) is used to set the forecasted power demand profile $W_k^* = \left(P_d^*(k+1), P_d^*(k+2) \dots, P_d^*(k+H_p)\right)$ as system disturbances, where its element P_d^* is computed based on the predicted velocity V_k^* and vehicles' dynamics (1)-(3). Moreover, let $\Delta y(k+i) = y(k+i) - r(k+i)$, the original cost function (17) can be reformulated into the following quadratic form:

$$J'(k) = \sum_{i=1}^{H_p} (\Delta y(k+i)^T Q(k+i) \Delta y(k+i) + u(k+i-1)^T R(k+i-1) u(k+i-1)) \quad (19)$$

where Q and R denote the corresponding penalty matrices. As a result, by using the quadratic programming (QP) solver, the k-th optimal control sequence $U_{opt,k} = \left(u_1(k), u_2(k), \dots, u_{H_p}(k)\right)$ can be obtained by minimizing the cost function (19) subject to constraints (18).

- Multiple working modes

The control performance of MPC-based EMS (e.g. fuel economy, FCS lifetime prolongation etc.) is

highly dependent on the settings of penalty factors (ρ_1, ρ_2, ρ_3) and FC reference power $P_{fc_{ref}}$. In this study, the multi-mode EMS framework is achieved through using different sets of MPC control parameters. Specifically, following working modes are considered:

1) Normal working mode. Three sets of MPC control parameters are tuned according to the power requirements under corresponding driving patterns. Afterwards, benefiting from the periodically updated pattern identification results, one set of offline-tuned parameters is selected for online implementation to cope with corresponding driving condition. The offline MPC control parameter tuning process is introduced in the subsection 3.3.3.

2) SoC urgency mode. To prevent battery SoC deviating too much from its reference value, when SoC urgency event (namely $SoC < 0.6$ or $SoC > 0.8$) occurs, ρ_3 is set to ten times of its normal value to force SoC back to the operation range [0.6,0.8]. Note when SoC urgency event occurs, the control parameter setting is switched to the "SoC urgency" mode and remains unchanged until next DPR result updating time instant.

3) Start-up mode. Due to the lack of historical driving information, the DPR result is set as "unrecognized" in the first sampling phase (e.g. $t \in [1,150]$). During the start-up phase, the MPC control parameters are set in such way that the battery pack is used to supply the majority of external power demands while the FC only works when the SoC value is below 0.6.

3.3.3. Model Predictive Controller Parameter Design

In this section, the offline MPC control parameter design procedure is illustrated.

- Working flow of MPC control parameters tuning

To find the reasonable MPC control parameter setting for each driving pattern, the parameter tuning process is given in Fig. 7(a). It contains four main steps: 1) DP approach is implemented under each type of combined driving cycle to extract the global optimal results. 2) Afterwards, corresponding $P_{fc_{ref}}$ is obtained according to the statistical distributions of the DP-optimized FC working points. 3) Given the FC reference power and penalty factor candidates, several performance metrics (e.g. final SoC, H2 consumption, FC power dynamics etc.) of MPC-based EMS on the same driving cycles are compared with DP-based optimal results. 4) Based on their performance deviations, three penalty factors are tuned through trials and errors.

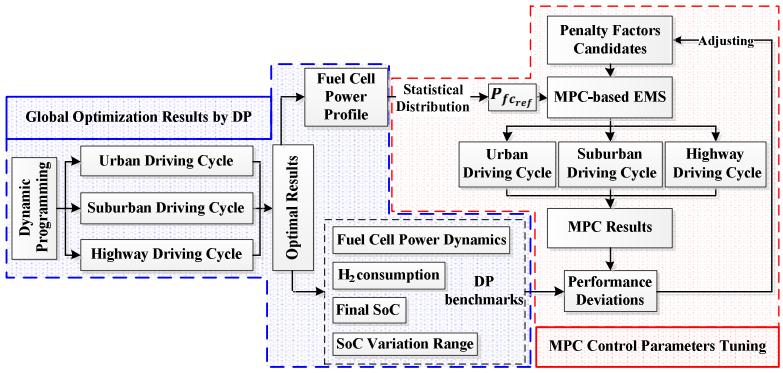

Fig. 7(a). Working flow of MPC control Parameters Tuning Process.

- Fuel cell reference power selection

During the DP optimization processes, the major objective in urban regions is to restrict the FC power transients against the fast dynamic power demands to extend the FCSs' lifetime. In contrast, in suburban and highway regions, the major objective is to urge FC working towards its high efficiency region to reduce the overall hydrogen consumptions. As can be seen, Fig.7 (b)-(d) depict

the DP-based optimization results under all driving conditions, where the corresponding optimal FC power distributions are summarized in Fig.7 (e).

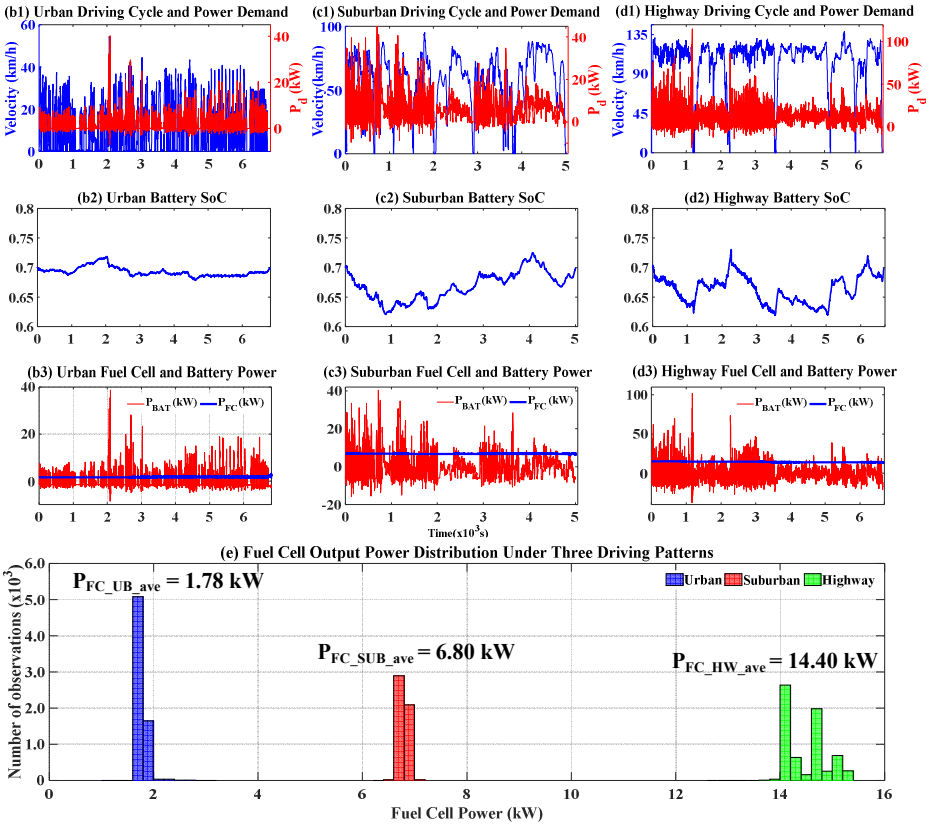

Fig.7 (b)-(e). DP-based optimization results under three driving patterns: (b1) urban driving cycles and the related power demand; (b2) battery SoC profile under urban driving condition; (b3) fuel cell and battery power profiles under urban driving condition; (c1) suburban driving cycles and the related power demand; (c2) battery SoC profile under suburban driving condition; (c3) fuel cell and battery power profiles under suburban driving condition; (d1) highway driving cycles and the related power demand; (d2) battery SoC profile under highway driving condition; (d3) fuel cell and battery power profiles under highway driving condition; (e) distribution of fuel cell working points under three driving patterns.

In urban regions, the optimal FC working points are distributed from 1.5 to 2.3 kW. In suburban regions, FC optimal working points are distributed within the range of 6.0 to 7.0 kW, while the optimal FC working range is 13.5 to 15.5 kW in highway regions. Consequently, the reference FC power for each driving pattern is set as the statistical average value, namely 1.78 kW (urban), 6.80 kW (suburban) and 14.40 kW (highway), respectively.

- Penalty factors tuning results

Based on the selected FC reference working points, the MPC penalty factors tuning results are given in Fig. 7(f)-(j). As seen from Fig. 7(f), after using the tuned penalty factors (red curve), the FC power transients under urban regions is greatly reduced compared to the MPC controller with non-tuned penalty factors (green curve). Similarly, as shown in Fig. 7(g) and (h), after penalty factor tuning, the variation of FC output power is restricted within a relatively narrow range and most of FC operating points are located in the high efficiency region.

Furthermore, the performance gaps among MPC-based strategies and DP-based benchmark are summarized in table III. Note “MPC-T” and “MPC-N” respectively denote the MPC-based EMSs with tuned and non-tuned penalty factors. m_{equ,H_2} denotes the equivalent H2 mass consumption, where the final battery SoC deviation from the initial value (0.7) is taken into consideration [14]. As can be seen, after using the tuned penalty factors, the MPC-based EMS obtains very similar

performance compared to DP benchmark. In addition, as shown in Fig. 7(i), with tuned MPC parameters, the largest performance gap on equivalent H2 consumption compared to the DP benchmark is only 0.14%. Moreover, as shown in Fig. 7(j), taken DP performance as comparison basis, the average FC power transients obtained by non-tuned MPC controller is from 6.259 to 26.999 times of DP basis, whereas this value declined significantly (1.008 to 1.111 times) after using the tuned MPC parameters. Consequently, it can be confirmed that the MPC penalty factors are well tuned, where the optimized MPC control parameters are given in table III. At each DPR result updating moment, one set of offline-tuned control parameters is selected to cope with the corresponding real-time driving pattern.

Fig.7 (f)-(j). EMS performance comparison before/after MPC penalty factor tuning: (f) performance comparison under urban driving condition; (g) performance comparison under suburban driving condition; (h) performance comparison under highway driving condition; (i) fuel economy discrepancy vs. DP benchmark; (j) fuel cell power transients discrepancy vs. DP benchmark.

TABLE III. MPC Performance Gaps against DP benchmark before/after parameter tuning

		UB			SUB			HW		
		DP	**MPC-T**	**MPC-N**	**DP**	**MPC-T**	**MPC-N**	**DP**	**MPC-T**	**MPC-N**
SoC_N		0.7000	0.7021	0.7032	0.7000	0.7123	0.7102	0.7000	0.7021	0.7131
m_{equ,H_2}(g)		135.10	135.20	135.71	418.30	418.90	422.29	1302.50	1302.71	1313.62
$\overline{\lvert\Delta P_{fc}\rvert}$ (w/s)		1.41	1.42	35.29	13.32	13.43	83.39	11.01	12.23	106.42
Opt. MPC parameters	(ρ_1,ρ_2,ρ_3)	**(1,2,100)**			**(1,1,60)**			**(1,0.2,54)**		
	$P_{fc_{ref}}$	**1.78 kW**			**6.80 kW**			**14.40 kW**		

IV. Simulation Results and Analysis

In this section, the performance of the proposed EMS is validated by simulation studies.

4.1 Evaluation on Pattern Identification Performance

The effectiveness of the proposed MC driving pattern recognizer is validated under three multi-pattern test cycles (namely test cycle I, II and III), where the number of MC state s and the total

MC time scale N_T are respectively set as 16 and 5 in this test.

- Evaluation results on test cycle I and II

To reveal the basic correctness of the proposed DPR approach, its performance is evaluated under test cycle I and II. As depicted in Fig. 8(a) and (e), the two test cycles contains eight identical standard driving cycles, which are extracted from the offline database (in section 3.1.2) for benchmark TPMs estimation.

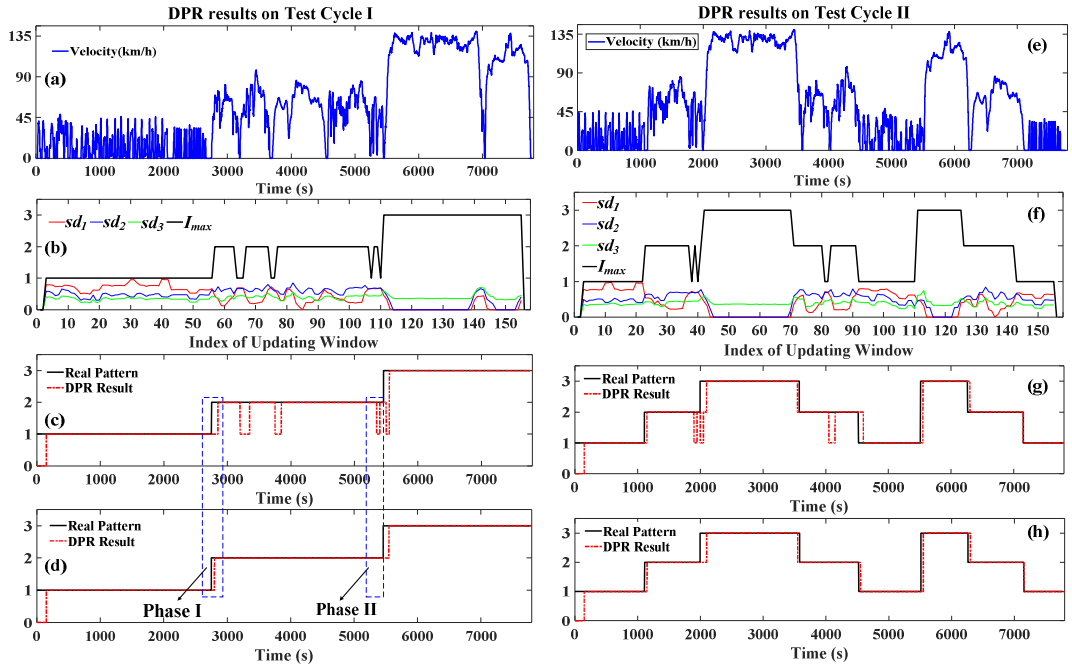

Fig. 8 (a)-(h). DPR results on test cycle I, II. Fig (a) and (e): Multi-pattern speed profile. Fig (b) and (f): Similarity quantification results. Fig (c) and (g): DPR results without complementary rules. Fig (d) and (h): DPR results with complementary rules.

Moreover, the similarity quantification results of the online estimated TPMs against the offline benchmark TPMs are given in Fig. 8 (b) and (f). The red, blue, and green curves respectively denote the obtained similarity degrees $(\mathrm{sd}_1, \mathrm{sd}_2, \mathrm{sd}_3)$ towards three pre-defined patterns and the black curve denotes the index of the largest element within the similarity vector. Since the length of update window $\mathrm{L_u}$ is 50s and the length of test cycle is 7767s, the DPR results are thus updated 156 times for the entire trip. Furthermore, the corresponding DPR results are given in Fig. 8(c), (d) and (g), (h). Overall, based on $\mathrm{I_{max}}$, the proposed approach can generate reasonable DPR results when external driving condition is stable. However, as shown in Fig.8 (c) and (g), mis-recognitions are more likely to occur when $\Delta \mathrm{SD_{max}} \leq \varepsilon_{\mathrm{SD}}$. In contrast, the DPR performance improved significantly after using the complementary rules (e.g. Phase I and II in Fig.8 (d)). Besides, the DPR result is set as "unrecognized (0)" during the first 150s since there are not enough historical data for DPR during the start-up phase. By comparing the pattern identification results under two test cycles, it can be confirmed that the concatenating sequence of the standard cycles would not bring significant DPR performance discrepancy.

- Evaluation results on test cycle III

As shown in Fig. 8(i), to further verify the DPR performance, eight driving cycles, which are not used for the benchmark TPMs estimation, are concatenated to form test cycle III.

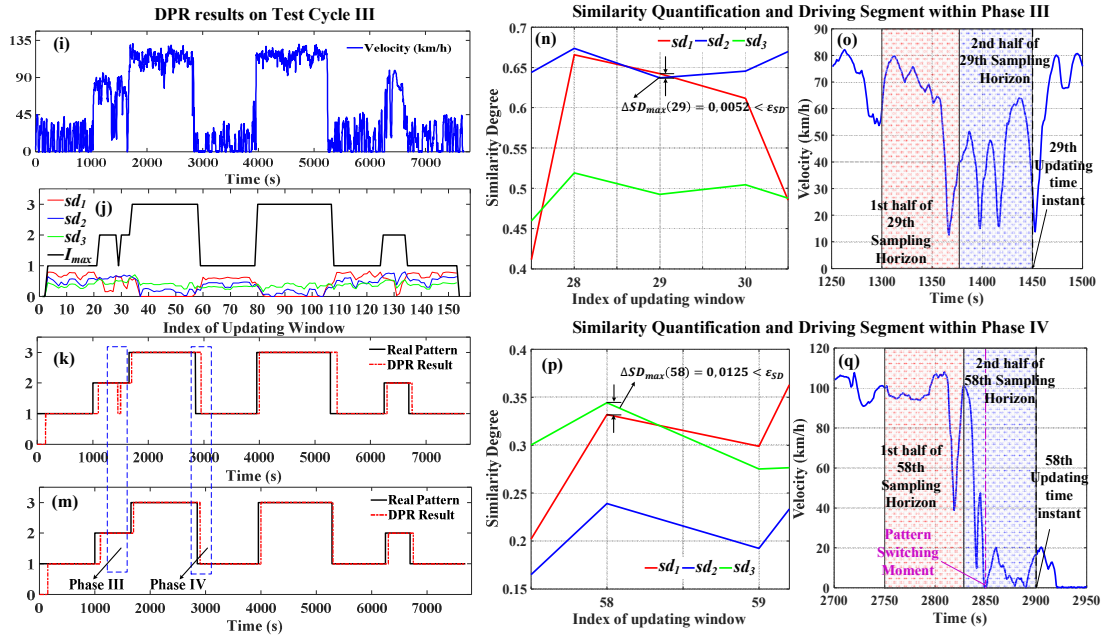

Fig. 8 (i)-(q): DPR results on test cycle III. Fig (i): Multi-pattern speed profile. Fig (j): Similarity quantification results. Fig (k): DPR results without the complementary rules. Fig (m): DPR results with the complementary rules. Fig (n)-(q) driving segments and similarity quantification results within phase III and IV.

Overall, as shown in Fig. 8(j)-(m), the MC pattern recognizer can generate the reasonable pattern separation results, indicating the effectiveness of the proposed method in handling the newly encountered driving conditions. Moreover, after using the complementary rules, the DPR performance enhanced from two perspectives: 1) the risks of the mis-recognition are reduced; 2) the latency before correctly recognizing the upcoming pattern is decreased.

For example, as shown in Fig. 8(n), the obtained similarity degree $\mathrm{sd}_1(29)$ is larger than $\mathrm{sd}_2(29)$ but their discrepancy (0.0052) is smaller than the threshold value $\varepsilon_{\mathrm{SD}} = 0.05$. Consequently, if without the complementary rules, the DPR result is set to "urban" since $\mathrm{I}_{\max}(29) = 1$, which causes the driving pattern mis-recognition, as shown in phase III of Fig. 8(k). In contrast, as shown in Fig. 8(o), there is no vehicle stop (zero-speed) event within the second half of 29th sampling horizon. According to the complementary rules shown in Fig. 6(b), current DPR result is set to "suburban" so that the pattern mis-recognition can be avoided, as shown in phase III of Fig. 9(m). Similarly, as shown in Fig. 8(p), due to $\mathrm{I}_{\max}(58) = 3$, the 58th DPR result is set to "highway" if without the complementary rules, leading to the pattern identification delay, as shown in phase IV of Fig. 8(k). In contrast, within the second half of 58th sampling horizon (Fig.8 (q)), three times of vehicle stop event are detected $(\mathrm{NoS} > 1)$. According to the complementary rules shown in Fig. 6(d), the 58th DPR result is set to "urban", leading to the acceleration of pattern identification, as shown in phase IV of Fig. 8(m).

TABLE IV. DPR Accuracy Comparison with/without Complementary Rules $(s = 16$ and $N_T = 5)$

	Test cycle I	**Test cycle II**	**Test cycle III**
Without complementary rules	93.55%	92.89%	92.32%
With complementary rules	98.16%	95.55%	94.97%
Accuracy Improvement	**+4.61%**	**+2.66%**	**+2.65%**

Table IV summarizes the DPR accuracy results under three test cycles. As can be seen, without complementary rules, the MC recognizer can achieve over 92.00% DPR accuracy on three test cycles. After using the complementary rules, additional 2.65% to 4.61% accuracy improvement can

be obtained, indicating the proposed complementary rules can enhance the DPR performance when $\Delta SD_{max} \leq \varepsilon_{SD}$. Overall, the 94.97% to 98.16% DPR accuracy indicates the proposed MC pattern recognizer can effectively separate the real-time driving patterns.

- DPR accuracy impacts brought by s and N_T

Note the setting on s and N_T would greatly affect the performance of the proposed DPR approach. Therefore, a sensitivity analysis is presented to reveal the impacts on DPR accuracy brought by different s and N_T. Corresponding numerical results are given in table V.

TABLE V. DPR Accuracy Comparison with Different Parameter Configurations

Parameter Settings		Test cycle I	Test cycle II	Test cycle III
$s = 16$	$N_T = 1$	88.19%	86.98%	91.64%
	$N_T = 2$	92.90%	92.89%	92.31%
	$N_T = 3$	94.87%	94.87%	92.32%
	$N_T = 4$	97.49%	95.52%	92.98%
	$N_T = 5$	98.16%	95.55%	94.97%
$s = 36$	$N_T = 1$	86.87%	85.88%	91.66%
	$N_T = 2$	89.50%	89.81%	91.66%
	$N_T = 3$	93.44%	92.23%	90.99%
	$N_T = 4$	93.44%	92.23%	90.99%
	$N_T = 5$	94.09%	93.54%	90.99%

As can be seen, the proposed method can obtain higher DPR accuracy when s is set to 16. If the MC size continues to increase, more observations are required to guarantee the completeness of the online estimated TPMs. In other words, the limited amount of driving data within the fixed sampling horizon $(L_s = 150s)$ makes the enlarged TPMs fail to fully characterize the (v-a) transition behaviors of recent driving segments, thus leading to the decrement of DPR accuracy. Furthermore, a larger N_T can contribute to the higher DPR accuracy (except for the results on test cycle III when $s = 36$). According to (11), a larger N_T enables more real-time identified TPMs for similarity quantification. In this case, the sensitivity towards the abnormal similarity quantification results would be decreased by using the average similarity degree, thus leading to the overall enhanced DPR accuracy. However, when N_T exceeds 5 seconds, such accuracy increment can be neglected. Consequently, when $s = 16$ and $N_T = 5$, the optimal DPR accuracy can be obtained under three test cycles. Therefore, such parameter configuration is used in the following tests.

4.2 Evaluation and Discussion on Multi-mode Energy Management Strategy

In this subsection, the performance of the proposed multi-mode EMS is evaluated through the comparisons with benchmark energy management strategies.

- Benchmark Energy Management Strategies Description

The performance of DP strategy is regarded as the upper benchmark, where the battery SoC is restricted within $[0.6,0.8]$ and the initial SoC value is set to 0.7. Additionally, a single-mode MPC-based strategy is introduced as the lower benchmark, where its FC power reference value is set as the best FCS efficiency working point, namely $P_{fc_{ref}} = P_{\eta_{max}}$. Besides, to cope with the unknown driving conditions, its penalty factors are tuned to mainly keep the battery SoC not deviating too much from the initial (reference) value (0.7).

- Evaluation Results on multi-pattern driving cycles

Five multi-pattern driving cycles are used for performance evaluation, where the comparative results under combined cycle I and II are given in detail.

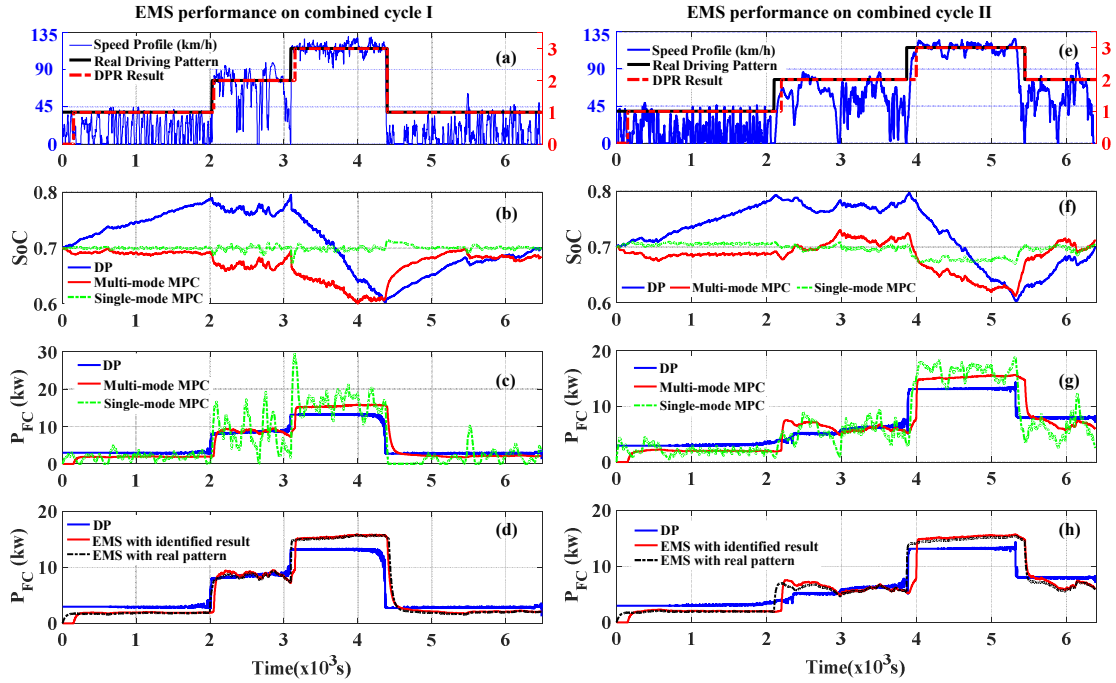

Fig. 9. EMS evaluation results on combined cycle I and II: (a) and (e) speed profiles and the related driving pattern information; (b) and (f) battery SoC trajectory comparison with benchmark strategies; (c) and (g) fuel cell output power comparison with benchmark strategies; (d) and (h) impacts on fuel cell power profiles brought by driving pattern identification errors.

As displayed in Fig. 9(a), the combined cycle I is a 6489s-long multi-pattern driving cycle, which consists of urban, suburban and highway driving conditions. The real driving pattern is plotted in black solid curve and the pattern identification result is given in red dashed curve. Overall, the MC pattern recognizer can achieve 97.05% DPR accuracy, where the errors are mainly caused by the identification delays during pattern switching phases. Besides, Fig. 9(b) depicts the battery SoC traces of three EMSs, where the DP strategy charges battery pack in urban regions to prepare for the peaking power demands in the following suburban and highway regions. Regarding the multi-mode EMS, the battery SoC is limited strictly around 0.7 in urban regions, while the battery energy is used in a relatively flexible manner in other regions. In addition, the single-mode EMS keeps SoC strictly around 0.7 during the entire trip. Moreover, the FC power comparison results are given in Fig. 9(c), where DP strategy urges FC working at specific power level under each driving pattern with few power transients. Similarly, the multi-mode EMS urges FC working towards different set points in a relatively stable manner. In contrast, the single-mode EMS results in much more FC power transients and on-off cycles, which could be harmful to the overall durability of FCS. Furthermore, Fig. 9(d) depicts the impacts on FC power caused by DPR errors, where the FC power profile of a multi-mode MPC controller with real driving pattern information (100% accuracy) is marked with black dashed format. Regarding the multi-mode EMS with pattern identification results, the FC power switching delay can be observed at each real pattern switching moment. When the external driving conditions become stable, their performance discrepancies are insignificant. Besides, as shown in Fig. 9(e)-(h), similar evaluation results can be found under the combined cycle II.

- Performance comparison and analysis

Table VI summarizes the numerical EMS evaluation results on five driving cycles. Note SoC_N is the final battery SoC value, $\overline{|\Delta P_{fc}|}$ is the absolute value of average FC power changing rate, m_{H_2} is the actual hydrogen consumption. Besides, the abbreviation “MPC-S” denotes the single-mode

EMS, "MPC-R" and "MPC-M" refer to the multi-mode MPC controller equipped with real driving pattern and the online DPR results, respectively. As can be seen, as a global optimization strategy, DP approach can result in the least amount of equivalent H2 consumption and the smallest FC power transients on all test cycles. In contrast, compared to the MPC-S strategy, the MPC-M strategy can reduce (1) the equivalent H2 consumption by 2.07% to 3.26% and (2) the FC power transients by 87.75% to 88.98% under five cycles, implying the improved fuel economy and the reduced risk of FCS performance degradations caused by frequent load changing. Furthermore, by comparing the results of MPC-R and MPC-M strategies, the DPR errors could slightly increase the equivalent H2 consumption by 0.06% to 1.30%.

TABLE VI. Numerical EMS evaluation results on five testing cycles.

Type	Road information	Metrics	DP	MPC-R	MPC-M	MPC-S
Combined Cycle I (CYC_I)	**Type: "UB + SUB +HW +UB"**	SoC_N	0.7000	0.6998	0.6844	0.7010
		m_{H_2} (g)	**474.30**	479.21	480.50	502.10
	DPR accuracy = 97.05%	m_{equ,H_2} (g)		**479.50**	**486.02**	**501.72**
		$\overline{\lvert\Delta P_{fc}\rvert}$(w/s)	**9.07**	**9.87**	**9.99**	**89.71**
Combined Cycle II (CYC_II)	**Type: "UB + SUB +HW +SUB"**	SoC_N	0.7000	0.7149	0.7133	0.7030
		m_{H_2} (g)	**552.10**	566.10	566.51	576.1
	DPR accuracy = 96.26%	m_{equ,H_2} (g)		**560.84**	**561.85**	**575.03**
		$\overline{\lvert\Delta P_{fc}\rvert}$(w/s)	**8.89**	**9.58**	**9.63**	**87.40**
Combined Cycle III (CYC_III)	**Type: "UB + SUB +HW +SUB+UB"**	SoC_N	0.7000	0.7067	0.7086	0.7012
		m_{H_2} (g)	**488.90**	503.7	504.60	512.70
	DPR accuracy = 96.24%	m_{equ,H_2} (g)		**501.34**	**501.63**	**512.25**
		$\overline{\lvert\Delta P_{fc}\rvert}$(w/s)	**9.85**	**10.03**	**10.59**	**86.48**
Combined Cycle IV (CYC_IV)	**Type: "UB + SUB +HW +UB"**	SoC_N	0.7000	0.7055	0.7066	0.7012
		m_{H_2} (g)	**527.02**	541.10	542.05	553.62
	DPR accuracy = 94.95%	m_{equ,H_2} (g)		**539.14**	**539.66**	**553.18**
		$\overline{\lvert\Delta P_{fc}\rvert}$(w/s)	**8.27**	**8.83**	**8.95**	**79.27**
Combined Cycle V (CYC_V)	**Type: "UB + SUB +HW +UB"**	SoC_N	0.7000	0.6956	0.6966	0.7011
		m_{H_2} (g)	**450.40**	458.50	459.50	476.60
	DPR accuracy = 96.61%	m_{equ,H_2} (g)		**460.08**	**460.73**	**476.25**
		$\overline{\lvert\Delta P_{fc}\rvert}$(w/s)	**9.89**	**10.41**	**10.53**	**93.09**

To further evaluate the performance of the proposed multi-mode strategy, a brief analysis on battery lifetime is conducted in the following part. As the energy storage/buffer within the hybrid powertrain, the durability of the onboard battery pack has great impacts on the operation safety and drivability of the FCHEVs. In this study, the battery output power is controlled by the EMS. However, inappropriate battery operations would accelerate its aging process, thus leading to the shortened lifetime. To simplify the evaluation process, it is assumed that the battery pack is brand new, the operation temperature is fixed at 25℃ and the initial SoC is 0.7. Two evaluation criteria for battery lifetime are introduced, namely the battery current c-rate and the SoC operation range, where the first metric is to describe the battery charge/discharge rate while the second one indicates whether the battery is over-charge (or over-discharge).

TABLE VII. Battery Current C-Rate (RMS value) and the SoC operation range comparison under five combined driving cycles

Metric	EMS	CYC_I	CYC_II	CYC_III	CYC_IV	CYC_V
I_{bat} C-Rate	MPC-S	1.0860	0.8121	0.8379	0.7667	1.2030
	MPC-M	1.1438 (+5.32%)	0.8446 (+4.00%)	0.8586 (+2.47%)	0.8064 (+5.18%)	1.2605 (+5.04%)
SoC Range	MPC-S	[0.6721,0.7133]	[0.6839,0.7154]	[0.6842,0.7148]	[0.6841,0.7154]	[0.6737,0.7115]
	MPC-M	[0.6010,0.7015]	[0.6119,0.7307]	[0.6187,0.7287]	[0.6067,0.7243]	[0.6141,0.7267]

Table VII summarizes the comparative results of the root mean square (RMS) value of battery

current c-rate and the SoC operation range under five combined testing cycles (marked as CYC_I to CYC_V). As can be seen, compared to the MPC-S strategy, the MPC-M strategy enlarges the battery current C-rate by 2.47% to 5.32%, implying the slightly higher battery charge/discharge rate. Therefore, the power losses on the battery internal resistance would increase and the rising temperature would intensify the side reactions within the battery cell and accelerate the fatigue of the active material crystal lattice, which would shorten the battery lifetime [37]. The reason for this phenomenon is that the control parameters for MPC-M strategy are optimized to limit the FC power transients for extending the FCSs' lifetime. Correspondingly, the battery pack is required to work more actively for handling the external power demand variations, thus leading to the enlarged battery charge/discharge rate. Moreover, both strategies can maintain the SoC within the predefined range [0.6, 0.8], implying a safe battery operation environment, where the relative small variation range of DC bus voltage is beneficial to reduce the control complexity of motor driving system for real applications.

In summary, compared to the single-mode strategy, the proposed multi-mode strategy can achieve (1) over 87.00% decrement on FC power transients and (2) at least 2.07% saving on hydrogen consumption. Although the battery durability could be slightly compromised, the significant performance improvement, especially on the FCS lifetime extension, brought by the multi-mode strategy is consistent with the initial EMS design objective. Furthermore, in face of the changeable driving conditions, the operation and maintenance cost of the FCS could be largely reduced by the proposed strategy, which should be regarded as the major advantage regarding the real implementation of the proposed EMS.

V. Conclusion

This paper presents a multi-mode energy management strategy for fuel cell hybrid electric vehicles. In the supervisory level, a novel Markov driving pattern recognizer is proposed, which can categorize the real-time measured driving segment into one of three predefined modes. Afterwards, one set of offline-tuned MPC control parameters is selected according to the pattern identification results. In the local optimization level, based on the specified control parameters, a multi-objective model predictive controller can generate the desirable control decisions considering the velocity prediction results. Overall, with the periodically updated pattern identification results, the proposed control strategy can adapt to the changeable driving conditions automatically. Validation results show the proposed Markov driving pattern recognizer can achieve 94.97% to 98.16% identification accuracy. Moreover, compared to the single-mode benchmark strategy, the proposed multi-mode strategy can significantly reduce over 87.00% fuel cell power transients as well as save 2.07% to 3.26% hydrogen consumption. This indicates the enhanced fuel cell system durability as well as the improvement on fuel economy. In future works, data fusion techniques will be considered for supplying a more reasonable way of combining online TPM similarity quantification results with multiple sets of pre-optimized MPC control parameters.

Reference

[1]. K. Palmer, J.E. Tate, Z. Wadud, J. Nelthorp. Total cost of ownership and market share for hybrid and electric vehicles in the UK, US and Japan. Appl. Energy. Vol. 209, Jan. 2018, Pages 108-119.

[2]. Y. Zhou. A. Ravey, MC. Péra. A survey on driving prediction techniques for predictive energy management of plug-in hybrid electric vehicles, J. Power Sources, Volume 412, 2019, Pages 480-495.

[3]. W. Ke, S. Zhang, X. He, Y. Wu, J. Hao. Well-to-wheels energy consumption and emissions of electric vehicles: Mid-term implications from real-world features and air pollution control progress. Appl. Energy. Vol. 188, Feb. 2017, Pages 367-377.

[4]. R. Ma, T. Yang, E. Breaz, Z. Li, P. Briois, F. Gao. Data-driven proton exchange membrane fuel cell degradation predication through deep learning method. Appl. Energy. Vol. 231, Dec. 2018, Pages 102-115.

[5]. N.Sulaiman, M.A.Hannan, A.Mohamed, P.J. Ker, E.H. Majlan, W.R.Wan Daud. Optimization of energy management system for fuel-

cell hybrid electric vehicles: Issues and recommendations. Appl. Energy, Vol. 228, Page: 2061-2079. Oct. 2018.
[6]. W. Shabbir, S.A. Evangelou. Threshold-changing control strategy for series hybrid electric vehicles. Appl. Energy. Vol. 235, Feb. 2019, Pages 761-775.
[7]. Y. Hung, Y. Tung, C. Chang. Optimal control of integrated energy management/mode switch timing in a three-power-source hybrid powertrain. Appl. Energy, Vol. 173, Jul. 2016, Pages: 184-196.
[8]. A. Ravey, B. Blunier, A. Miraoui. Control Strategies for Fuel-Cell-Based Hybrid Electric Vehicles: From Offline to Online and Experimental Results. IEEE Trans.Veh. Technol. Vol. 61(6), Page: 2452-2457. May 2012.
[9]. F. Peng, Y. Zhao, T. Chen, X. Zhang, W. Chen, D. Zhou, Q. Li. Development of robust suboptimal real-time power sharing strategy for modern fuel cell based hybrid tramways considering operational uncertainties and performance degradation. Appl. Energy. Vol. 226. Sep. 2018. Pages 503-521.
[10]. Q. Li, H. Yang, Y. Han, M. Li, W. Chen. A state machine strategy based on droop control for an energy management system of pemfc-battery-supercapacitor hybrid tramway, Int. J. Hydrogen Energy 41 (36) (2016) 16148–16159.
[11]. H. Zhang, X. Li, X. Liu, J. Yan. Enhancing fuel cell durability for fuel cell plug-in hybrid electric vehicles through strategic power management. Appl. Energy. Vol. 241, May. 2019, Pages 483-490.
[12]. V. Larsson, L. Johannesson, B. Egardt. Analytic Solutions to the Dynamic Programming Subproblem in Hybrid Vehicle Energy Management. IEEE Trans. Veh. Technol, Vol. 64, No. 4, Pages: 1458-1467, Apr. 2015.
[13]. O. Sundstrom, L. Guzzella, "A generic dynamic programming Matlab function," in IEEE CCA ISIC, 2009, pp. 1625–1630.
[14]. D. Zhou, A. Al-Durra, F. Gao, A. Ravey, I. Matraji, M. G. Simoes. Online energy management strategy of fuel cell hybrid electric vehicles based on data fusion approach. J. Power Sources. Vol. 366, Page: 278-291, Oct 2017.
[15]. S. Ahmadi, S.M.T. Bathaee, Multi-objective genetic optimization of the fuel cell hybrid vehicle supervisory system: Fuzzy logic and operating mode control strategies, Int. J. Hydrogen Energy, Volume 40, Issue 36, 2015, Pages 12512-12521.
[16]. H. Li, A. Ravey, A. N'Diaye, A. Djedir. A novel equivalent consumption minimization strategy for hybrid electric vehicle powered by fuel cell, battery and supercapacitor. J. Power Sources, Vol. 395 Feb. 2018, pp. 262-270.
[17]. C. Yang, S. Du, L. Li, S. You, Y. Yang, Y. Zhao. Adaptive real-time optimal energy management strategy based on equivalent factors optimization for plug-in hybrid electric vehicle. Appl. Energy. Vol. 203, Oct. 2017, Pages 883-896.
[18]. A. Rezaei, J.B. Burl, A. Solouk, B. Zhou, M. Rezaei, M. Shahbakhti. Catch energy saving opportunity (CESO), an instantaneous optimal energy management strategy for series hybrid electric vehicles. Appl. Energy. Vol. 208, Dec. 2017, Pages 655-665.
[19]. C. Sun, X. Hu, S. J. Moura, F. Sun. Velocity Predictors for Predictive Energy Management in Hybrid Electric Vehicles. IEEE Trans. Control Syst. Technol., Vol. 23(3), May 2015.
[20]. S. Xie, X. Hu, Z. Xin, J. Brigton. Pontryagin's Minimum Principle based model predictive control of energy management for a plug-in hybrid electric bus. Appl. Energy. Vol. 236, Feb. 2019, Pages 893-905.
[21]. S. Zhang, R. Xiong, F. Sun. Model predictive control for power management in a plug-in hybrid electric vehicle with a hybrid energy storage system. Appl. Energy. Vol. 185, Jan. 2017, Pages 1654-1662.
[22]. C. Xiang, F. Ding, W. Wang, W. He. Energy management of a dual-mode power-split hybrid electric vehicle based on velocity prediction and nonlinear model predictive control. Appl. Energy. Vol. 189, Mar. 2017, Pages 640-653.
[23]. H. Wang, Y. Huang, A. Khajepour, Q. Song. Model predictive control-based energy management strategy for a series hybrid electric tracked vehicle, Appl. Energy, Volume 182, Nov. 2016. Pages 105-114.
[24]. C.H. Zheng, G.Q. Xu, Y.I. Park, W.S. Lim, S.W. Cha. Prolonging fuel cell stack lifetime based on Pontryagin's Minimum Principle in fuel cell hybrid vehicles and its economic influence evaluation. J. Power Sources, 248 (2014), pp. 533-544.
[25]. X. Huang, Y. Tan, X. He. An Intelligent Multifeature Statistical Approach for the Discrimination of Driving Conditions of a Hybrid Electric Vehicle. IEEE Trans. Intell. Transp. Syst., Vol. 12, No. 2, Jun. 2011.
[26]. S. Zhang, R. Xiong. Adaptive Energy Management of a Plug-in Hybrid Electric Vehicle Based on Driving Pattern Recognition and Dynamic Programming. Appl. Energy, Vol. 155, Oct. 2015. Pages 68-78.
[27]. R. Zhang, J. Tao, H. Zhou. Fuzzy Optimal Energy Management for Fuel Cell and Supercapacitor Systems Using Neural Network Based Driving Pattern Recognition. IEEE Trans. Fuzzy Syst., Vol.27 (1), Page: 45-57, July 2018.
[28]. K. Song, F. Li, X. Hu, L. He, W. Niu, S. Lu, T. Zhang. Multi-mode energy management strategy for fuel cell electric vehicles based on driving pattern identification using learning vector quantization neural network algorithm, J. Power Sources, Vol. 389, 2018.
[29]. H. Xie, G. Tian, G. Du, Y. Huang, H. Chen, X. Zheng, T. H. Luan. A Hybrid Method Combining Markov Prediction and Fuzzy Classification for Driving Condition Recognition. IEEE Trans. Veh. Technol., vol. 67 (11), Nov. 2018.
[30]. Z. Chen, L. Li, B. Yan, B. Yan, C. Yang, C.M. Martinez, D. Cao. Multimode Energy Management for Plug-In Hybrid Electric Buses Based on Driving Cycles Prediction. IEEE Trans. Intell. Transp. Syst., VOL. 17, NO. 10, Pages: 2811-2821, OCT 2016.
[31]. A. Ravey, N. Watrin, B. Blunier, D. Bouquain, A. Miraoui. Energy-Source-Sizing Methodology for Hybrid Fuel Cell Vehicles Based on Statistical Description of Driving Cycles. . IEEE Trans. Veh. Technol., vol. 60 (9), Nov. 2011.
[32]. L. Guzzella, A. Sciarretta. Vehicle Propulsion Systems: Introduction to Modeling and Optimization. Berlin: Springer-Verlag, pp. 14-18, 2005.
[33]. MC. Péra, D. Hissel, H. Gualous, C. Turpin. Electrochemical Components. John Wiley & Sons, Inc. 2013.
[34]. V. H. Johnson. Battery performance models in ADVISOR. J Power Sources. Vol. 110, Issue 2, Pages 321-329, Aug 2002.
[35]. D. P. Filev, I. Kolmanovsky, "Generalized markov models for real-time modeling of continuous systems," IEEE Trans. Fuzzy Syst, vol. 22, no. 4, pp. 983–998, 2014.
[36]. I. V. Kolmanovsky, D. P. Filev. Stochastic optimal control of systems with soft constraints and opportunities for automotive applications. 2009 IEEE Control Applications, (CCA) & Intelligent Control, (ISIC).
[37]. S. Zhang, R. Xiong, J. Cao. Battery durability and longevity based power management for plug-in hybrid electric vehicle with hybrid energy storage system. Appl. Energy. Vol. 179, Oct. 2016, Pages 316-328.